Atmospheric
Measurement
Techniques
Discussions

Radiative transfer simulations and observations of infrared spectra in the presence of polar stratospheric clouds: Detection and discrimination of cloud types

Christoph Kalicinsky[1], Sabine Griessbach[2], and Reinhold Spang[3]

[1]Institute for Atmospheric and Environmental Research, University of Wuppertal, Germany
[2]Forschungszentrum Jülich, Jülich Supercomputing Centre, JSC, Jülich, Germany
[3]Forschungszentrum Jülich, Institut für Energie und Klimaforschung, Stratosphäre, IEK-7, Jülich, Germany

Correspondence: C. Kalicinsky (kalicins@uni-wuppertal.de)

Abstract. Polar stratospheric clouds (PSCs) play an important role for the spatial and temporal evolution of trace gases inside the polar vortex due to different processes, such as chlorine activation and NOy redistribution. As there are still uncertainties in the representation of PSCs in model simulations, detailed observations of PSCs and information on their type (nitric acid trihydrate (NAT), supercooled ternary solution (STS), and ice) are desirable.

5   The measurements inside PSCs by the airborne infrared limb sounder CRISTA-NF (CRyogenic Infrared Spectrometers and Telescope for the Atmosphere – New Frontiers) during the RECONCILE (Reconciliation of essential process parameters for an enhanced predictability of Arctic stratospheric ozone loss and its climate interactions) aircraft campaign showed a spectral peak at about $816\,\mathrm{cm^{-1}}$. This peak is shifted compared to the peak at about $820\,\mathrm{cm^{-1}}$, which is known to be caused by small NAT particles. To investigate the reason for this spectral difference we performed a large set of radiative transfer simulations of infrared limb emission spectra in the presence of various PSCs (NAT, STS, ice, and mixtures) for the airborne viewing

10   geometry of CRISTA-NF. NAT particles can cause different spectral features in the region $810 - 820\,\mathrm{cm^{-1}}$. The simulation results show that the appearance of the feature changes with increasing median radius of the NAT particle size distribution from a peak at $820\,\mathrm{cm^{-1}}$ to a shifted peak and, finally, to a step-like feature in the spectrum. Based on this behaviour we defined different colour indices to detect PSCs containing NAT particles and to subgroup them into three size regimes: small

15   NAT ($\leq 1.0\,\mathrm{\mu m}$), medium NAT ($1.5 - 4.0\,\mathrm{\mu m}$), and large NAT ($\geq 3.5\,\mathrm{\mu m}$). Furthermore, we developed a method to detect the bottom altitude of a cloud by using the cloud index (CI), a colour ratio indicating the optical thickness, and the gradient of the CI. Finally, we applied the methods to observations of the CRISTA-NF instrument during one local flight of the RECONCILE aircraft campaign and found STS and medium sized NAT.

1 Introduction

20

Polar stratospheric clouds (PSCs) form inside the cold polar vortices in both hemispheres in winter. They have a major influence on the ozone chemistry and thus the ozone depletion in the stratosphere (Solomon, 1999). PSCs are classified into three different types: supercooled ternary solution (STS) droplets, nitric acid trihydrate (NAT), and ice particles (e.g. Lowe and MacKenzie, 2008). The formation and existence of these different types is largely temperature dependent. Solid ice particles

25 can only exist below the frost point $T_{\mathrm{frost}} \approx 188$ K, whereas NAT particles are thermodynamically stable at temperatures below $T_{\mathrm{NAT}} \approx 195$ K. The liquid STS droplets form from binary H_2SO_4-H_2O droplets at temperatures below the dew point of HNO_3 $T_{\mathrm{dew}} \approx 192$ K by the uptake of HNO_3 (see e.g. Peter and Grooß, 2012, and references therein).

PSCs directly and indirectly influence the spatial distribution of trace gases relevant for ozone depletion in different ways. Due to heterogenous reactions on the cold particle surfaces chlorine is activated from its reservoir species, mainly HCl and $ClONO_2$,

30 and the chlorine radicals catalytically destroy ozone (e.g. Solomon, 1999). NAT particles can grow to larger sizes, which then leads to a sedimentation of the particles and thus to a permanent removal of HNO_3 from the stratosphere (denitrification) (e.g. Fahey et al., 2001; Molleker et al., 2014). This denitrifaction slows down the deactivation of chlorine and thus enhances the ozone loss (e.g. Waibel et al., 1999; Peter and Grooß, 2012).

Because of these different processes and due to the fact that many models rely on rather simple parametrisations, the simulation

35 of PSCs and related processes is difficult and partly accompanied with larger uncertainties (see Spang et al. (2016, 2018) for more detailed discussions). Thus, as many observations of PSCs as possible and a detailed discrimination into the different particle types are necessary to enhance the understanding of the relevant processes and reduce the uncertainties. Infrared limb emission sounder build a good basis for such kind of studies (e.g. Spang and Remedios, 2003; Höpfner et al., 2006).

Besides the derivation of volume mixing ratios of several trace gases, infrared limb emission sounder such as CRISTA (CRyo-

40 genic Infrared Spectrometers and Telescopes for the Atmosphere; Offermann et al., 1999; Grossmann et al., 2002), CRISTA-NF (CRyogenic Infrared Spectrometers and Telescope for the Atmosphere – New Frontiers; Kullmann et al., 2004), and MIPAS-Envisat (Michelson Interferometer for Passive Atmospheric Sounding - Envisat; Fischer et al., 2008) are well suited to detect clouds of different composition. Spang et al. (2001) established a simple and effective way for cloud detection based on the radiance ratio of two specific spectral regions. The first one is dominated by CO_2 emissions (around $792 \ \mathrm{cm}^{-1}$) and the second

45 one by the emissions of aerosol (around $833 \ \mathrm{cm}^{-1}$). This detection method was then succesfully used in various studies and for different satellite and airborne instruments (e.g. Spang and Remedios, 2003; Spang et al., 2002, 2005, 2008, 2015; Höpfner et al., 2006; Kalicinsky et al., 2013). Furthermore, the infrared spectra exhibit different spectral features or radiance behaviours in the presence of polar stratospheric clouds of different type. Spang and Remedios (2003) presented a sharp peak-like feature at around $820 \ \mathrm{cm}^{-1}$ observed by the CRISTA instrument in the Antarctic winter for the first time. They attributed this feature

50 to HNO_3-containing particles. Höpfner et al. (2006) showed that the feature can be best reproduced in simulations by using refractive index data for β-NAT particles. The authors showed that the color ratio method derived by Spang and Remedios (2003) that exploits the peak-like feature for detection is able to identify PSCs containing small NAT particles (radii $< 3 \ \mu$m). By means of a large set of radiative transfer simulations Spang et al. (2012, 2016) developed a detection and discrimination

method for PSCs. Besides the feature at 820 cm^{-1}, the method also uses further spectral behaviours such as a radiance de-
crease from around 830 cm^{-1} towards larger wavenumbers (around 950 cm^{-1}) that occurs in the case of ice to distinguish
different PSC types. Spang et al. (2018) finally presented a climatology of the PSC composition for the whole MIPAS-Envisat
observation time period (2002 – 2012) based on this method.

During the RECONCILE campaign (Reconciliation of essential process parameters for an enhanced predictability of Arctic
stratospheric ozone loss and its climate interactions; von Hobe et al., 2013) a slightly different type of spectral feature was
observed by the infrared limb emission sounder CRISTA-NF in the presence of PSCs. The campaign took place in Kiruna,
Sweden, in January to March 2010 and the high-flying research aircraft M55-Geophysica carried out a number of flights with
a huge set of different instruments to study the polar vortex and related scientific topics such as PSCs, ozone chemistry, or
mixing processes. CRISTA-NF was one of the operated instruments and the instrument is able to detect clouds and distinguish
different types of PSCs. During the first five flights of the campaign (17.01. – 25.01.2010) CRISTA-NF detected PSCs around
the aircraft. The infrared spectra measured inside the clouds show a noticeable spectral feature at about 816 cm^{-1}. This feature
is slightly shifted towards smaller wavenumbers compared to the typical spectral feature at 820 cm^{-1}, which is caused by
very small NAT particles. Another spectral feature, a step-like or shoulder-like behaviour of the radiance in the spectral region
810 – 820 cm^{-1}, has been observed by the ballon-borne instrument MIPAS-B in January 2001 (Höpfner et al., 2002) and the
airborne instrument MIPAS-STR during the ESSENCE campaign in December 2011 (Woiwode et al., 2016). Woiwode et al.
(2016) suggested highly aspherical medium/large sized (median radius 4.8 µm) NAT particles causing the change of the NAT
signature. Thus, the appearance of the spectral feature seems to depend on the particle size distributions of the NAT particles,
especially on the median radius. This motivated the following study of the relationship between the appearance of the feature
(typical, shifted, and step-like) and the corresponding particle size distribution aiming at an improved detection method for
PSCs containing NAT particles. Especially the possibility to detect larger NAT particles is important, because they play the
major role for the denitrification of the stratosphere (Fahey et al., 2001; Molleker et al., 2014), and thus for the whole ozone
chemistry (e.g. Waibel et al., 1999; Peter and Grooß, 2012). New insights and an improvement of the detection method is also
interesting for measurements of other infrared limb emission sounder such as MIPAS-Envisat, where data for a long observa-
tion period (about 10 years) and both hemispheres are available. For this purpose a large variety of different PSCs with respect
to the composition, spatial dimensions, and particle size distributions of the PSC particles was simulated and analysed.

The paper is structured as follows. In Sect. 2 the CRISTA-NF instrument and the radiative transfer code are described and the
setup used for the simulations is explained. The results of the simulations are presented and analysed in Sect. 3. The derived
methods are applied to the CRISTA-NF measurements in Sect. 4. Finally, the main results are summarised in Sect. 6.

2 Methods and setup

The radiative transfer simulations were performed using the viewing geometry and spectral properties of the airborne infrared
limb sounder CRISTA-NF. The background atmosphere used for the simulations is a polar winter atmosphere with conditions
suitable for the formation of polar stratospheric clouds. The simulations itselves were performed using the radiative transfer

code JURASSIC. This section describes the CRISTA-NF instrument, the JURASSIC radiative transfer code, the setup used for the simulations, and the different cloud scenarios that were investigated.

2.1 CRISTA-NF istrument

90   The airborne CRISTA-NF instrument is a successor of the satellite instrument CRISTA. CRISTA-NF measures the thermal emissions of the atmosphere in the mid-infrared region from 4 to 15 μm in an altitude range from flight altitude (up to 20 km) down to approximately 5 km. A detailed description of the design of the cryostat and the optical system is given by Kullmann et al. (2004). The calibration procedure and some improvements for the RECONCILE campaign are described by Schroeder et al. (2009) and Ungermann et al. (2012), respectively.

95   CRISTA-NF uses a Herschel telescope and a tiltable mirror to scan the atmosphere from flight altitude down to approximately 5 km. The incoming radiance is then spectrally dispersed by two Ebert-Fastie grating spectrometers (e.g., Fastie, 1991). These two spectrometers have different spectral resolving powers of $\frac{\lambda}{\Delta\lambda} \approx 1000$ and 500, respectively, and are therefore denoted as high resolution spectrometer (HRS) and low resolution spectrometer (LRS). In this study we focus on the spectral range that is covered by the two channels LRS 5 ($850 - 965$ cm^{-1}) and LRS 6 ($775 - 865$ cm^{-1}). The vertical sampling of the LRS

100   during one altitude scan is typically between 100 and 200 m with finer sampling at higher altitudes and a wider one at lower altitudes due to mounting and instrument conditions. The field of view (FOV) is very small with 3 arcmin (about 300 m at 10 km tangent height; Spang et al., 2008). The radiance is finally measured using liquid helium cooled semiconductor detectors (Si:Ga) that are operated at a temperature of 13 K. These low temperatures enable fast measurements of one spectrum in about one second.

105   2.2 JURASSIC

For the simulations of the CRISTA-NF infrared spectra in the presence of PSCs we used the Juelich Rapid Spectral Simulation Code (JURASSIC) (Hoffmann, 2006). It is a fast radiative transfer model for the mid-infrared spectral region. It was used in numerous studies analysing infrared limb and nadir measurements, including MIPAS-Envisat (Hoffmann et al., 2005, 2008), CRISTA-NF (Hoffmann et al., 2009; Weigel et al., 2009), and the nadir sounder AIRS (Hoffmann and Alexander, 2009), and

110   to simulate 2-D trace gas and temperature retrievals for a proposed new infrared limb instrument named PREMIER IRLS (Preusse et al., 2009; Hoffmann and Riese, 2010). For fast radiative transfer calculations, JURASSIC applies a spectrally averaging approach by using the emissivity growth approximation (EGA) (Gordley and Russel III, 1981; Marshall et al., 1994) and precalculated look-up tables. The look-up tables were calculated by the line-by-line model reference forward model (RFM; Dudhia, 2017) and take into account the spectral resolution of the instrument to be investigated.

115   JURASSIC has been compared to the line-by-line models RFM and KOPRA for selected spectral windows and shows good agreement (Griessbach et al., 2013). JURASSIC was extended with a scattering module that allows for radiative transfer simulations including single scattering on aerosol and cloud particles (Griessbach et al., 2013). The optical properties of the particles, extinction coefficient, scattering coefficient, and phase function, required for the radiative transfer simulations with

Atmospheric
Measurement
Techniques
Discussions
Open Access
EGU

scattering, can either be calculated with an internal Mie code assuming spherical particles, or can be taken from databases for
120 non-spherical particles. The scattering module was successfully used in different studies (Griessbach et al., 2014, 2016, 2020).

2.3 Simulation setup

The simulation setup can be divided into three parts: the instrument part, the atmosphere part, and the cloud scenarios. The instrument part includes the viewing geometry and the spectral properties of the airborne infrared limb emission sounder CRISTA-NF. In the atmosphere part we describe the background atmosphere that is used for the simulations. All different
125 types of polar stratospheric clouds with respect to the position and thickness of the cloud as well as the composition (NAT, STS, ice) are summarised in the cloud scenario section.

2.3.1 Instrument properties

The two important spectral regions that are necessary to analyse infrared spectra with respect to polar stratospheric clouds are $785 - 840$ cm^{-1}, because of the cloud index (CI) and the NAT signature, and the region $940 - 965$ cm^{-1}, because of an ice
130 signature. The spectral resolving power used in the simulations is $\frac{\lambda}{\Delta\lambda}$ = 536 at a reference wavelength of 12.5 µm (800 cm^{-1}) (see Weigel, 2009). The spectral sampling of the CRISTA-NF measurements is about 0.0065 µm that corresponds to an average of 0.42 cm^{-1} for the wavelength range $785 - 840$ cm^{-1} and 0.59 cm^{-1} for the region $940 - 965$ cm^{-1}. These values have been considered in the calculation of the look-up tables for JURASSIC. We used an observer alitude of 18.4 km, which is the maximum average flight altitude during the RECONCILE flights of interest. However, the average altitudes of all flights only
135 differ by a few hundred meters (18.1 to 18.4 km). The observations were simulated in the altitude range from observer altitude down to 10 km. The vertical sampling used for the simulations was 100 m. Tab. 1 summarises these properties.

2.3.2 Atmospheric setup

For the background atmosphere we used polar winter conditions to get representative simulations. Most information are taken from the MIPAS reference polar winter climatology by Remedios et al. (2007). For some constituents we made updates and
140 here we focused on the winter 2009/2010, especially on the January 2010. There are two reasons for this choice: 1. A large variety of PSCs have been observed in the Arctic in this winter. 2. The CRISTA-NF observations of PSCs during RECONCILE took place in January 2010. The updates are summarised in the following part.
Two very important parameters of the atmosphere for the simulation of infrared spectra are temperature and CO_2 volume mixing ratios (VMR). In order to have a temperature profile that is representative for a situation where many different PSCs
145 can occur we focused on the observation period of PSCs during the RECONCILE aircraft campaign (17 to 25 January 2010). The temperature profile was derived using ERA-Interim reanalysis data (Dee et al., 2011). An average profile in the region of the CRISTA-NF observations north of Kiruna ($67° - 78°$ N, $10° - 35°$ E) was used for the background atmosphere. Additonally, we used the corresponding pressure profile from ERA-Interim reanalysis data. The CO_2 VMR we derived from the reconstructed CO_2 product by Diallo et al. (2017) for January 2010. The profile is a zonal average in the latitude region of interest. The

150   profiles were extended to larger altitudes following the slope of the climatology. As PAN (peroxyacetyl nitrate) is not included
in the climatology, we took a mean profile derived from CRISTA-NF observations (see Ungermann et al. (2012) for retrieval
description) in the region around Kiruna between end of January and begin of March. Unfortunately, there are no retrieval
results for PAN during the PSCs flights available. However, the derived profile is in a good agreement with published MIPAS-
Envisat observations for October to December 2003 in the corresponding latitude region (Glatthor et al., 2007) and also with

155   the average profile in 2007/08 in the latitudinal band $60° - 90°$ (Pope et al., 2016). For CFC-11, CFC-113, HCFC-22, SF_6, and
COF_2 we updated the climatological profiles to 2010 values by using information of tropospheric values (Bullister, 2011) as
well as satellite observations by ACE-FTS (Boone et al., 2013) and in-situ observations carried out by the HAGAR instrument
(Riediger et al., 2000; Werner et al., 2010) onboard the M55-Geophysica during RECONCILE.

In order to save computation time we restricted the number of trace gases to a minimum by just using those gases that have a

160   noticeable contribution to the total radiance in the two analysed spectral regions. The trace gases have been selected seperately
for the two spectral regions. For the region 785–840 cm^{-1} we used 13 trace gases: CO_2, HNO_3, $ClONO_2$, O_3, H_2O, HNO_4,
CCl_4, CFC-11, HCFC-22, CFC-113, PAN, ClO, NO_2. The simulations in the region 940–965 cm^{-1} included 9 trace gases:
CO_2, HNO_3, O_3, H_2O, CFC-11, PAN, SF_6, NH_3, COF_2. A summary of the trace gases, their sources, and the spectral region
in which they have been considered is given in Tab. 2.

165   **2.4   Cloud scenarios**

Two parameters that were largely varied to investigate different situations are the position and the thickness of the PSCs. The
PSC position was varied between a minimum cloud bottom height (CBH) of 13 km and a maximum top height of 30 km. In
the case of the thickness we used the values 0.5, 1.0, 2.0, 4.0, and 8.0 km. The bottom height is shifted in 1 km steps up to 20
km (slightly above flight altitude) and in 2 km steps above for each thickness value as long as the cloud top height (CTH) is

170   lower or equal to 30 km.

PSCs consisting of NAT particles are the most interesting ones for this study, because of their impact on the NOy redistribution.
Thus, the largest part of the simulations were performed for this particle type. The two parameters varied for the NAT scenarios
are the median radius of the particle size distribution and the number density of the particles. The different particle size
distributions for all cases (also ice, STS) were described by a log-normal distribution

175

$$\frac{\mathrm{d}N}{\mathrm{d}r} = \frac{N_0}{\sqrt{2\pi}\ln(\sigma)r}e^{-\frac{(\ln(r)-\ln(\mu))^2}{2\ln^2(\sigma)}}, \tag{1}$$

where r is the radius, N_0 is the number density, μ is the median radius, and σ is the width. The width is constant at $\sigma = 1.35$
and we varied the median radius between 0.5 and 8.0 µm. For the calculation of the number densities and thus the particle size
distributions we used different HNO_3 VMRs from 1 to 15 ppbv under the assumption that one HNO_3 molecule is converted to
one NAT molecule. The calculations were done for typical conditions for the lower stratosphere with 193 K and 60 hPa.

180   Furthermore, we also simulated PSCs using bimodal NAT particle distributions. The median radius of the first mode varied
from 0.5 to 2.5 µm and was combined with a second mode, where radii larger than in the first mode were used. The total
HNO_3 VMR was always 10 ppbv and the ratios between first and second mode were 70/30, 50/50, and 30/70. Here, we only

simulated two bottom altitudes at 13 and 17 km and three different thicknesses 1, 4, and 8 km.

Additonally, we performed simulations for the PSC particle types STS and ice. The volume densities used for these simulations

185 range from $0.1 - 10.0$ µm³/cm³ and from $0.1 - 100.0$ µm³/cm³ for STS and ice, respectively. The median radii were varied

between 0.1 and 1.0 µm for STS and between 1.0 and 10.0 µm for ice. In the case of STS we simulated three different mixtures

of H_2SO_4/HNO_3 with wt% of 2/48, 25/25 and 48/2.

Finally, we simulated mixed NAT/STS clouds. Here, we also used only the bottom altitudes at 13 and 17 km and the different

thicknesses 1, 4, and 8 km like in the case of bimodal NAT. Furthermore, we concentrated on the small and medium size NAT

190 particles up to 3.5 µm and used three different HNO_3 VMRs of 5, 10, and 15 ppbv. We combined these NAT scenarios with

STS scenarios using wt% 2/48, volume densities of 5 and 10 µm³/cm³, and radii of 0.1, 0.3, and 1.0 µm.

The parameter ranges for all cloud scenarios are summarised in Tab. 3. The refractive indices for ice, NAT, and the STS

mixtures were taken from Toon et al. (1994), Biermann (1998) with refinement in Höpfner et al. (2006), and Biermann et al.

(2000), respectively. The total number of scenarios was 16224 (NAT: 9240, STS: 3192, ice: 2352, and mixtures (bimodal NAT

195 and NAT/STS): 1440).

3 Results of the simulations

The following section deals with the analyses of the simulation results. The analyses can be devided into three parts. 1. The

shift of the NAT feature; 2. The detection of PSCs and the identification of the PSC types NAT and ice; 3. The determination

of the bottom altitude of the clouds.

200 ### 3.1 Shift of the NAT feature

The appearance of the spectral feature that is observed in infrared limb spectra in the presence of polar stratospheric clouds

consisting of NAT particles depends on the median radius of the particle size distribution (more accurate it depends on the scat-

tering radius, which itself depends on the median radius and the width σ). With increasing median radius the shape transforms

from the well known pronounced peak at about 820 cm^{-1} to a peak, which is slightly shifted towards smaller wavenumbers,

205 and, finally, to a step-like feature. Figure 1 illustrates this behaviour and the dependency of the appearance on the median

radius. The spectra shown in Fig. 1 have been scaled such that the radiance in the spectral range $832.0 - 834.0$ cm^{-1} is equal to

one for all spectra. The example spectrum for the smallest median radius of 0.5 µm (yellow colour) exhibits a clear pronounced

peak at about 820 cm^{-1}. For slightly larger median radii ($1.0 - 3.5$ µm) the peak shifts to smaller wavenumbers and becomes

less pronounced (orange colours). When the median radius is even larger the spectral feature transforms to a step-like feature

210 that shows a steep radiance decrease from about 811 cm^{-1} to 826 cm^{-1}. The magnitude of this decrease largely diminishes

with increasing median radius.

This behaviour and thus the dependency of the appearance of the feature on the median radius can be explained by the different

contributions of extinction and scattering to the total observed radiance enhancement caused by the PSCs. These contributions

largely depend on the median radius of the particles. The real and the imaginary part of the refractive index of β-NAT are shown

215 in Fig. 2 in black and red, respectively. The imaginary parts illustrates the emission and absorption characteristic of the NAT particles whereas the real part shows the scattering behaviour. The imaginary part shows a distinct peak at about $820\,\mathrm{cm^{-1}}$. As the emission is the major contribution when only small particles are present the simulated spectra in case of small NAT only show this peak. For large particles the scattering of radiance into the line of sight is the most important mechanism. Since the real part exhibits a step-like structure, the simulated spectra for large NAT particles show this step, too. Medium size particles

220 have contributions of both mechanisms with different proportions depending on the size of the particles. Thus, the shape of the simulated spectra resemble a combination of both parts (real and imaginary) of the refractive index. As a consequence the peak shifts to smaller wavenumbers with increasing particle size until it transforms to a step-like signature.

The spectral feature with all its versions in the region $810-820\,\mathrm{cm^{-1}}$ is a unique signature that only occurs in the presence of NAT PSCs and will be used for the detection of such type of PSCs. Other PSCs consisting of STS or ice do not show such

225 a feature as exemplarily shown in Fig. 1 for two examples with light blue (STS) and dark blue (ice) colours. In contrast to the other PSC types ice shows the largest relative difference between the region $832.0-834.0\,\mathrm{cm^{-1}}$ and the second spectral range of our simulations ($940-965\,\mathrm{cm^{-1}}$). Only NAT PSCs consisting of particles with very small radii can also achieve large differences. This spectral behaviour in the case of ice will further be used to detect ice PSCs.

3.2 Detection of NAT

230 ### 3.2.1 Unimodal pure NAT

The detection of clouds using infrared limb spectra typically uses the cloud index (CI) (e.g Spang et al., 2001, 2002, 2008). The CI is the radiance ratio between a spectral region dominated by CO_2 at around $792\,\mathrm{cm^{-1}}$ and a second spectral region dominated by aerosol or cloud particles at around $833\,\mathrm{cm^{-1}}$. For the analysis of the airborne observations by CRISTA-NF we used the two windows $791.0-793.0\,\mathrm{cm^{-1}}$ and $832.0-834.0\,\mathrm{cm^{-1}}$. Because of the different viewing geometries and

235 instrument properties, the first window is smaller defined than that typically used for satellite observations (Spang et al., 2008). In cloud free conditions the CI value is typically large (around 10). When clouds or larger aerosol loads are in the line of sight of the instrument the CI significantly drops to smaller values depending on the optical thickness of the cloud.

The detection of NAT particles inside clouds is based on the characteristic spectral behaviour in the region $810-820\,\mathrm{cm^{-1}}$. In former studies a NAT index, the radiance ratio between the spectral region of the typical NAT feature ($819-821\,\mathrm{cm^{-1}}$) and

240 the region of the CO_2-peak ($788-796\,\mathrm{cm^{-1}}$), was introduced to detect PSCs containing small NAT particles (e.g Spang and Remedios, 2003; Höpfner et al., 2006; Spang et al., 2012, 2016, 2018). Here, we define the NAT index-1 as the radiance ratio between the two regions $819-821\,\mathrm{cm^{-1}}$ and $791-793\,\mathrm{cm^{-1}}$ and use the same smaller window in the region of the CO_2-peak as for the CI. In a scatter plot of the NAT index-1 versus the CI spectra simulated for small NAT particles separate from spectra simulated for larger NAT particles and other types of PSCs (Fig. 3 a)). Nearly all simulations with NAT particles $< 3\,\mathrm{\mu m}$ lie

245 above the region of the simulations for STS and ice clouds, which is marked by the solid black line. Thus, NAT particles within this size range can be detected and discriminated using NAT index-1.

In order to detect PSCs containing larger NAT particles and to make the estimation of the size range of the particles more

distinct we introduce two new NAT indices here. The NAT index-2, which is defined as the radiance ratio between $815 - 817$ cm^{-1} and $791 - 793$ cm^{-1}, focuses on the shifted NAT feature that occurs for larger particles than that producing the non-shifted feature. Figure 3 b) shows the scatter plot of the NAT index-2 versus the CI. In contrast to the NAT index-1 now the results for PSCs with larger NAT particles (up to 4 μm) also lie above the simulations for STS and ice (black separation line). Additonally, for different particle median radii the distance to the separation line changes when going from NAT index-1 to index-2 in an opposite way. In the case of very small particles the distance becomes smaller as the spectral region used for the detection moves away from the center of the typical NAT peak. For larger particles the behaviour is opposite and the distance enlarges as the spectral region moves to the center of the shifted NAT peak. This opposite behaviour can be seen in Fig. 3 c) where the difference between NAT index-1 and index-2 is shown on the y-axis. It is obvious that the simulations for the two smallest radii (0.5 an 1.0 μm) behave opposite to the simulations for larger radii.

Lastly, we introduce NAT index-3, which is defined as the radiance ratio between $810 - 812$ cm^{-1} and $825 - 827$ cm^{-1}, to detect PSCs containing even larger NAT particles. This ratio enables the discrimination of a step-like feature from a peak and a more or less constant radiance in the complete spectral range as it is the case for STS and ice. Figure 3 d) shows the scatter plot of NAT index-3 against the CI. The simulation results for small NAT particles (≤ 1.0 μm) have a NAT index-3 smaller than for the simulations results for STS and ice. A large part of the simulation results for larger NAT particles show a NAT index-3 that is larger than for the simulation results for STS and ice. By using this ratio also NAT particles with radii > 4 μm separate from the other simulation results and are consequently detectable.

In total the three different NAT indices enable the detection of PSCs containing NAT particles and allow for a classification of the NAT particles in different size regimes. The detection and discrimination of NAT can be divided into three different cases: Case-1 (small NAT): Detection of NAT using NAT index-1 and the difference NAT index-1 – index-2 is above separation line; Case-2 (medium NAT): Detection of NAT using NAT index-2 and the difference NAT index-1 – index-2 is below separation line; Case-3 (large NAT): No Detection of NAT using NAT index-1 and index-2 (both below separation line), but the NAT index-3 is above the separation line. Figure 4 shows the proportion between the detected NAT spectra and the cloud spectra (spectra below a certain CI threshold) in each size bin of the simulations (0.5 – 8.0 μm) colour coded for the three different cases. In panel a) of Fig. 4 only observations with a CI below 5.0 are taken into account. Obviously, in case-1 (yellow colour) only NAT particles with a median radius of 0.5 or 1.0 μm are detected. The detection results in case-2 (orange colour) go from 1.5 μm up to 4.0 μm and the results in case-3 (yellow colour) all show median radii larger than or equal to 2.5 μm, whereby the radius 2.5 μm only occurs in a very small amount. Thus, the different cases all represent a specific size regime with no or little overlap to the other cases. Especially, the very small NAT particles (0.5 and 1.0 μm) can be completely distinguished from the particles with other median radii, since all of the detected spectra in this size range fall into case-1. The other two cases have overlap with each other.

The total detection capacity is also very good. For median radii up to 6.0 μm nearly all spectra that have been detected as cloud spectra can be detected as spectra influenced by NAT particles. Only for 2.5 and 3.0 μm a few cloud spectra cannot be identified as NAT spectra. These spectra all have a larger CI value (> 3.0, optically thinner) and for larger CI values the separation between NAT and the other PSC types degrades (compare Fig. 3). Thus, a small part of the cloud spectra influenced

by NAT cannot be distinguished from STS and ice. When the CI threshold value is reduced to 3.0, the detection itself and also the separation between the different size regimes improves, as shown in Figure 4 b). Now all spectra for median radii up to

285 $6.0\,\mu m$ are identified as NAT. Additionally the separation between the different sizes is now better and case-3 only detects radii $\geq 3.5\,\mu m$. Independent of the CI threshold value only a part of the simulations for the largest median radius of $8.0\,\mu m$ are detected as NAT (CI < 5.0: $\sim 30\%$; CI < 3.0: $\sim 40\%$). This is caused by the decreasing magnitude of the radiance decrease from $811\ cm^{-1}$ to $826\ cm^{-1}$ for increasing median radius (see Sect. 3.1). According to the different size ranges of the three cases, the cases are hereafter denoted as small NAT (sNAT: $\leq 1.0\,\mu m$), medium NAT (mNAT: $1.5 - 4.0\,\mu m$), and large NAT

290 (lNAT: $\geq 3.5\,\mu m$). Compared to the former method where only the NAT index-1 is used (e.g. Spang and Remedios, 2003; Höpfner et al., 2006; Spang et al., 2012, 2016, 2018) our new approach with three NAT indices enables an improved detection capacity as more NAT clouds can be detected. For our simulations the improvement is about a factor of 1.78 (approximately 190000 cloud spectra identified as NAT with all new indices and about 108000 spectra identified as NAT when only using index-1) for a CI < 3.0.

3.2.2 Mixed NAT/STS clouds

We additionally simulated mixed NAT/STS clouds to evaluate the influence on the spectra and especially the performance of our classification into different size regimes. Here, we only simulated a subset of all possible combinations, as the spectral behaviour for each median radius is very similar independent of e.g. the bottom altitude of the cloud or the thickness (see Sect. 2.4).

300 If STS is present in addition to NAT, the relative magnitudes of the spectral features caused by NAT particles get smaller and therefore the separation between these mixed clouds and STS is also restricted compared to a pure NAT cloud. Figure 5 a) shows example spectra for PSCs of pure NAT (solid lines in red for $0.5\,\mu m$ and blue for $1.0\,\mu m$) and PSCs with the same NAT and additionally STS (dashed lines) to illustrate this effect. In a scatter plot of the NAT indices versus the CI (compare Fig. 3 a) and b)) the simulation results for the NAT/STS mixtures are closer to the separation line or even below compared to pure NAT.

305 When the NAT detection and classification procedure (described in the previous subsection) is applied to the simulation results for the mixed clouds, the good discrimination between the small and medium size particles remains. This discrimination relies on the difference of NAT index-1 and index-2, where both indices are influenced in the same way. Therefore, the sign of the difference remains the same because this depends on the position of the spectral peak, which is not affected by the additional STS (see Fig. 5 a)). In some cases STS completely masks the spectral features caused by NAT and NAT is not detectable any

310 more. However, for a CI value below 3.0 more than 90% of the cloud spectra can still be identified as containing NAT. This value of 90% decreases with increasing CI and also will decrease with increasing STS volume density or decreasing HNO_3 VMR inside the PSC. In a nutshell, in mixed STS-NAT-clouds less scenarios are identified as containing NAT, because the STS reduces the amplitude of the characteristic NAT signature. But, if a scenario was classified as NAT, the size attribution remains as reliable as in the pure NAT scenarios.

3.2.3 Bimodal NAT clouds

In addition, we also simulated PSCs using bimodal NAT particle distributions with a main focus on the small and medium size particles and the separation between those. Here, also a subset of all possible combinations was simulated (see Sect. 2.4). The spectra simulated for the bimodal NAT particle size distributions are typically some kind of mixture of the spectra for the corresponding unimodal distributions, thereby the HNO_3 VMR ratio plays an important role. Figure 5 b) shows an example for a spectrum simulated for a bimodal NAT particle distribution (black line). The HNO_3 VMRs were 5 ppbv in each mode with median radii of 2.5 µm and 6.0 µm. The two corresponding spectra for the unimodal size distributions are shown in red and blue, respectively. Obviously, the spectrum for the bimodal size distribution is a mixture of the other two. When the HNO_3 ratio for both modes is changed to 70/30 or 30/70 the spectrum looks more like the spectrum for that unimodal size distribution that dominates the bimodal distribution because of more HNO_3 in the corresponding size range.

We applied our classification procedure also to these simulations for bimodal size distributions with the following results. When the first mode dominates (70% HNO_3), nearly all cloud spectra simulated for a median radius of 0.5 or 1.0 µm are still detected as sNAT (about 99% sNAT and 1% mNAT), and thus classified correctly. All spectra that are identified as cloud (CI < 3.0) are also identified as NAT containing PSCs. For a HNO_3 ratio of 50/50 or 30/70 the influence of the second mode increases such that more and more spectra are detected as mNAT and a small part as lNAT. In the case of the ratio 50/50 about 50.5% are classified as sNAT and 49.5% as mNAT and for a ratio of 30/70 21% are classified as sNAT, 77% as mNAT, and 2% as lNAT. When combined with larger NAT particles in the second mode (≥ 4 µm) a part of the cloud spectra (CI < 3.0) are not detected as NAT because neither a spectral peak nor a step-like behaviour can be detected (50/50: 0.5% and 30/70: 10%). However, these cases are only a few percent of all cloud spectra in our simulations. When the first mode has a median radius between 1.5 – 2.5 µm about 99% of the spectra are identified as mNAT (1% lNAT, when the median radius in the second mode is 5.0 or 6.0 µm) independent of the ratio of the HNO_3 VMRs. Furthermore, only a few per mille of the spectra identified as clouds cannot be classified as NAT containing PSCs. In total, our new classification scheme delivers very reasonable results even in the case of bimodal NAT particle size distributions.

3.3 Detection of ice

The detection of ice uses the fact that in the presence of ice a large radiance decrease from about 833 cm^{-1} to 949 cm^{-1} can be observed (compare Fig. 1). This clear decrease is only observed in the case of ice or in the presence of very small NAT particles. Spang et al. (2012, 2016) used this spectral behaviour to detect ice clouds in satellite measurements of MIPAS-Envisat. The authors used the brigthness temperature (BT) difference between the two spectral regions. Here, we adopt the method for the CRISTA-NF observations. Because of the different viewing geometry, spectral resolution and the different definition of the CI for the two instruments, the separation lines have to be newly defined. The spectral regions used for the BT difference are 832.0 – 834.0 cm^{-1} and 947.5 – 950.5 cm^{-1}. In a scatter plot of the BT difference against the CI, the simulated ice spectra clearly separate from other particle types (Fig. 6). Obviously, spectra that are influenced by ice clearly separate from STS and nearly all NAT particles when the cloud is optically thick enough (low CI). For larger CI values the separation gets smaller.

The only particle type that can produce similar values of the BT difference are very small NAT particles with median radii of 0.5 μm (yellow colours in Fig.6), but these particles can be safely filtered out with the method described before in Sect. 3.2.

350 Consequently, the BT difference is a very robust method to detect ice particles in PSCs.

3.4 Detection of STS

Unfortunately, the spectra for STS show neither a local spectral feature like the spectra for NAT nor a broadband spectral feature such as the spectra for ice. Thus, the detection of STS can not be achieved by using a unique spectral behaviour. In practice the detection procedure is as follows. Firstly, the NAT detection methods are used to detect observations of NAT particles and

355 to distinguish between the three size regimes. Secondly, the BT difference method is applied to the observations to detect ice. Finally, the observations inside PSCs that are neither detected as NAT nor as ice are categorised as STS. It is not necessarily the case that the spectra categorised as STS are solely influenced by STS. It is possible that NAT or ice also were present in the PSC but the additional amount of STS was enough to minimise the spectral features such that NAT or ice is not definitely detectable any more. Furthermore, the small amount of very large NAT particles that cannot be distinguished from STS and ice

360 will also fall in the category STS.

3.5 Bottom altitude of the PSCs

Further important quantities with respect to cloud detection are the vertical thickness and the position of the cloud defined by the top and bottom altitude. Here, we present a method to determine the bottom altitude of the observed cloud. The cloud index, which is used to detect optically thick conditions caused by clouds (or aerosol), shows characteristic vertical changes in

365 the presence of clouds. These changes are used for the detection of the cloud bottom altitude.

The left panel of Fig. 7 shows examples of CI altitude profiles for clouds with different vertical thicknesses. When the complete cloud is located below the flight altitude (yellow colour) the CI largely drops to low values when entering the cloud from above (or slightly above because of the FOV). In the case the flight altitude is inside the cloud the CI is already low at flight altitude. Then the CI typically further decreases with decreasing altitude inside the cloud and the minimum CI value is reached close to

370 the bottom altitude. Only in some cases when the vertical thickness is larger (4 km or 8 km) the CI minimum can be located somewhere inside the cloud. When leaving the cloud the CI increases again. These vertical changes of the CI can be best illustrated with the gradient of the CI (right panel in Fig. 7). Slightly above the cloud top the vertical gradient maximises and slightly below the cloud bottom the gradient reaches its minimum value. In contrast to the CI minimum, where larger deviations to the cloud bottom can occur, the minimum of the gradient is always slightly below the real bottom altitude of the cloud.

375 Figure 8 summarises the results for the simulated clouds with a bottom altitude below flight altitude. In the case of the CI minima (full circles) there are sometimes larger deviations from the real bottom altitude when the cloud is vertically thick (red and light blue full circles). The CI gradient minima (full diamonds) are always located close to the real bottom altitude, at the first or the second measurement below. The possibility to observe the gradient minimum at the second measurement below the cloud increases with decreasing altitude of the cloud, because the vertical extent in metres of the FOV is larger at lower

380 altitudes. In our simulations this occurs only at bottom altitudes of 13.0 and 14.0 km. In summary, the CI minimum and the

gradient minimum enclose the real bottom altitude. A large gap between the two minimum values indicates the observation of a cloud with a larger vertical thickness.

There are further restrictions for the determination of the bottom altitude. Firstly, when the cloud is optically too thick, a vertical change of CI can hardly be seen anymore. Therefore, the CI minimum and the gradient minimum cannot be used for

385 the detection of the bottom altitude of an optically thick cloud. A CI minimum value of 1.2 serves as a good threshold. Such low values of CI only occur for a part of the ice clouds simulated here but not for the NAT and STS clouds. Secondly, when the cloud is optically and vertically thin, the location of the cloud bottom is not detectable as well. In order to select only clouds that are optically thick enough for detection we used only simulation spectra with CI < 5.0.

4 Application to the CRISTA-NF measurements

390 This section shows the application of the methods derived from the simulations to observations by the CRISTA-NF instrument. We show results for the detection of the bottom altitude and the detection and discrimination of PSCs exemplarily for the RECONCILE local flight 3, which took place on 22.01.2010. The flight started in Kiruna (Sweden) and the whole flight was located northward of Kiruna inside the polar vortex.

4.1 Bottom altitude

395 During the RECONCILE local flight 3 the aircraft flew through PSCs. Thus, the CRISTA-NF instrument made measurements inside PSCs during a large part of the flight. The behaviour of the CI and the CI gradient can now be used to detect the bottom of the PSCs. Figure 9 shows the CI and the CI gradient for two selected altitude profiles that have been measured inside PSCs. These two profiles show the behaviour as expected from the simulations. In case of profile 102 (right panel in Fig. 9) the CI becomes smaller from flight altitude downwards as long as the measurements are inside the cloud (compare red and yellow

400 profile of CI in Fig. 7). The CI gradient shows the largest negative value one sampling step below the CI minimum. According to the simulation results the CI gradient minimum is located below the cloud whereas the CI minimum is located inside the cloud. Thus, in this example an accurate detection of the bottom altitude is possible (profile 102: ~17.3 – 17.4 km). In the case of profile 80 the behaviour of CI and CI gradient is very similar. Only the altitude difference between the CI minimum and the CI gradient minimum is larger than only one sampling step (profile 80: ~17.2 – 17.5 km). This can be caused by two effects.

405 Firstly, the PSC is inhomogeneous and this causes the increase of the CI above the CI gradient minimum which is supposed to be located directly below the PSC. Secondly, in the case of vertically largely extended clouds this behaviour is also observed in the simulations (compare Fig.7 blue curves). If the vertical extent is responsible for the difference between the two minima, this would suggest that the vertical extend is larger than 2 km. However, the difference between the two minima is only about 300 m. Thus, the detection of the bottom altitude, which is located between these two points, is still very accurate.

410 Figure 10 a) shows the cross section of the CI for the complete flight. During the middle section of the flight the aircraft crossed PSCs as can be seen by the low CI values (blue colours) at and directly below the flight altitude. Beneath this region the CI values are larger again, which indicates cloud free conditions below the PSCs. The green and the magenta line in Fig. 10 a) mark

the CI minima and the CI gradient minima, respectively. Only profiles where both minima could sufficiently be determined are considered. Similar to the results for the two selected profiles (compare Fig. 9) the two minima are primarily located in the

415   region between 17 and 17.5 km. Thus, for most profiles a good estimate of the bottom altitude of the cloud is achieved.

4.2   PSC classification

The measurements are now analysed with respect to the PSC type using the methods described in Sect. 3. During a large part of the flight numerous spectra below the bottom altitude of the cloud (see green and magenta lines in Fig. 10 a)) would be detected as PSC influenced spectra. This is expected as a large part of the line of sight (LOS) is still inside the PSC and, thus, the spectral

420   features caused by the PSC particles are visible in the spectra. Since the cloud bottom height was determined by the CI gradient method, we restricted the analysis of the altitude range between flight altitude and the CI gradient minima. Figure 10 b) shows the cross section of the detected PSC types. Additionally, only spectra with a CI value below 3.0 are considered (Fig. 10 b)). During the complete flight only medium sized NAT and STS were observed (orange and light blue colours in Fig. 10 b)). Figure 11 shows example spectra inside the PSCs at about 12:10 UTC, which show a shifted NAT feature at about 816 cm^{-1},

425   and thus a classification as mNAT is expected. The new method reliably detects spectra showing such a shifted NAT feature. Most of the observations detected as STS are located in the second half of the PSC observation from the flight altitude downwards. This is also in accordance with the spectra that have been measured in this region. These spectra (see Fig.11) show a clear shifted NAT feature only at altitudes a few hundred metres below flight altitude. Directly below the flight altitude the NAT feature can hardly be seen. This does not necessarily mean that no NAT was present in this altitude region, but the STS

430   contribution to the measured radiances was that large, thus all other particle type signatures were masked out. Additionally, the CI values in this region are lower directly below flight altitude (compare Fig. 10 a)) compared to the first part of the PSC. In addition to the smaller distance between the CI minima and the gradient minima in the second part of the PSC this suggests that the vertical extent of the cloud is smaller compared to the first part or that the PSC is optically thinner.

In summary the methods derived in Sect. 3 are able to give a complete picture of the observed PSC. The PSC and the bottom

435   altitude of the cloud are clearly detected and the new and improved detection method enables the classification of medium size NAT particles and STS during RECONCILE flight 3.

5   Discussion

Small NAT particles cause a distinct spectral peak in infrared limb emission spectra at about 820 cm^{-1}. This peak has already been observed in satellite measurements since the 1990's (Spang and Remedios, 2003; Höpfner et al., 2006). We showed with

440   our simulations that the appearance of the NAT feature changes with changing particle size. The spectral peak (small NAT) transforms to a shifted peak (medium NAT) and, finally, to a step-like behaviour of the spectrum (large NAT) with increasing median radius of the particle size distribution. This change is related to the different proportions to which scattering and absorption/emission contributes to the total radiance (see also Woiwode et al., 2016).

The different spectral features can be used to distinguish between different size regimes. Our new approach enables the dif-

Atmospheric
Measurement
Techniques
Open Access
EGU
Discussions

445   ferentation between small NAT (0.5 – 1.0 μm), medium NAT (1.5 – 4.0 μm), and large NAT ($\geq$ 3.5 μm). In contrast to the
former method where only one NAT index is used (detection of NAT < 3.0 μm) (see Spang and Remedios, 2003; Höpfner
et al., 2006; Spang et al., 2016) this improved method leads to a larger detection capacity as more NAT containing clouds
can be detected. A part of the medium sized particles (those when only NAT index-2 is above the separation line) and the
complete size range of large NAT particles are not detected with the former method. Probably this improvement will diminish

450   the discrepancy between NAT cloud observations by MIPAS-Envisat and the CALIOP instrument onboard CALIPSO in the
Northern hemisphere, where much more NAT was observed by CALIOP (the difference in the Southern hemisphere is much
smaller)(Spang et al., 2018). Consequently, this would conclude a larger probability for the formation of NAT clouds with
medium to large radii for the Northern hemisphere compared to Southern hemisphere conditions, which highlights a link to
different formation mechanisms and meteorological conditions fostering the formation of large or small NAT particles.

455   The derived methods can easily be adopted to analyse other observations like that of MIPAS-Envisat, as the spectral behaviour
in general is the same. The separation lines would need to be adjusted, because different instruments have different spectral
properties and viewing geometries. Thus, the new NAT detection method can be transfered to MIPAS-Envisat, but a set of sim-
ulations is necessary to do this. In the case of the ice detection we sucessfully transfered the method used for MIPAS-Envisat
(e.g. Spang et al., 2016) to the airborne geometry of CRISTA-NF and refined the separation lines.

460   In recent publications by Woiwode et al. (2016, 2019) a special step-like behaviour of infrared spectra in the presence of NAT
particles was intensively analysed and the authors simulated the observed spectra by the presence of large aspherical NAT parti-
cles. Woiwode et al. (2019) showed the large shoulder-like signature at about 820 cm^{-1} and flat radiance behaviour afterwards,
which they called hockey-stick signature, for an example observed by MIPAS-Envisat. The authors assigned this behaviour
to be characteristic for large aspherical NAT particles and developed a detection method for this type of spectrum. The main

465   criteria used for the detection are a difference in the integrated radiance between the window 817.5 – 818.5 cm^{-1} and 833.0 –
834.0 cm^{-1} above a certain value (to detect the step or shoulder) and a difference in the integrated radiance between the win-
dow 833.0 – 834.0 cm^{-1} and 960.0 – 961.0 cm^{-1} below a certain value (to detect the flat behaviour at larger wavenumbers).
Our simulations agree at the point that large spherical NAT particles (with unimodal distribution) typically show a step-like
behaviour but a decrease in the radiance towards larger wavenumbers (compare Fig. 1 reddish colours and Fig. 5 b) blue line),

470   and therefore do not show this hockey-stick signature. But some of our simulations for the bimodal NAT particle size distri-
butions show this typical behaviour. The spectrum in Fig. 5 for the bimodal NAT particle size distribution (black line) exhibits
no decrease in radiance from about 833 to 960 cm^{-1}. Furthermore, the step or shoulder is more pronounced compared to the
spectrum for the unimodal size distribution (blue line) and slighty shifted towards larger wavenumbers. Therefore, the radiance
decrease from 818 to 833 cm^{-1} increases. In our opinion, the spectral behaviour presented here is very similar to the spectra

475   of Woiwode et al. (2019) without using aspherical NAT particles at all. This suggest that large aspherical NAT particles are not
necessariliy the only possibility to observe such a kind of spectrum or spectral signature. Thus, the spectrum alone is possibly
not enough to definitely detect aspherical NAT particles. But a complete picture of the situation involving infrared emission
spectra, FSSP observations of the particle size distribution, and information on the HNO$_3$ budget together will presumably be
sufficent to make a clear decision.

480 Unfortunately, the differences used in the detection scheme by Woiwode et al. (2019) rely on absolute differences, which are not applicable for CRISTA-NF, because of the viewing geometries and spectral properties of the instruments. In order to analyse the detection scheme by Woiwode et al. (2019) in more detail simulations for the MIPAS-Envisat instrument are necessary, which is beyond the scope of this paper. However, the simulations for the CRISTA-NF instrument clearly show the effects of bimodal NAT particle size distributions on the infrared spectra and the possibility to obtain a hockey-stick signature.

6 Summary and conclusions

We performed a large set of radiative transfer simulations of infrared limb emission spectra in the presence of polar stratospheric clouds of different types (NAT, STS, ice). All simulations have been performed for the viewing geometry and spectral properties of the CRISTA-NF instrument. These simulations build a new data base that is used for the analysis of PSC spectra to develop and refine detection and discrimination methods.

490 We showed with our simulations that the NAT feature changes from a spectral peak at 820 cm^{-1} (small NAT) to a shifted peak (medium NAT) and, finally, to a step-like behaviour of the spectrum (large NAT) with increasing median radius. Based on this behaviour we developed an improved method to detect NAT particles, which for the first time allows the discrimination of three different size regimes: small NAT (0.5 – 1.0 µm), medium NAT (1.5 – 4.0 µm), and large NAT ($\geq$ 3.5 µm). This new detection method will also improve the analysis of other observations by infrared limb emission sounder such as MIPAS-

495 Envisat. The ice detection method was adopted from former studies (MIPAS-Envisat) and the separation lines were newly defined. Additionally, we developed a new method to detect the bottom altitude of the clouds. This method uses the gradient of the CI, which minimises shortly below the real bottom altitude. As the minimum of the CI itself is located inside the cloud (typically close to the bottom), these two quantities give a good estimate for the bottom altitude. This method can surely be transfered to other cloud observations such as cirrus clouds and aerosol layers and to other airborne instruments measuring

500 in the same wavelength region like e.g. GLORIA. A prerequisite for a sucessful usage of the method is a small FOV like that of CRISTA-NF. Larger FOVs will lead to a larger vertical averaging of the measurements and thus to a minimisation of the detection capabilities. This can already be seen for the CRISTA-NF instrument, where at lower altitudes (14 km and below) the minimum of the CI gradient can move further away from the real bottom altitude.

Finally, we applied the new methods to observations of CRISTA-NF during the RECONCILE local flight 3. The results show

505 a polar stratospheric cloud that has been crossed during the flight by the aircraft and extends downward to about 17 – 17.5 km. The PSC contained NAT particles, which could be classified to be of medium size (1.5 – 4 µm) as in the spectra always a shifted NAT feature has been observed. This shifted feature is safely detected by the new method.

Moreover, using the method developed here a new data set of PSC observations and classification can be obtained. This new data set will help to improve the results of trace gas retrievals in the presence of PSCs by integrating realistic PSC extinction

510 spectra into the retrieval process. Furthermore, the gained data will help to improve the representation of PSCs in model simulations.

Code and data availability. The JURASSIC code is available at https://github.com/slcs-jsc/jurassic-scatter. The simulation results are available at https://datapub.fz-juelich.de/slcs/cloud-spectra/psc-crista-nf/. The CRISTA-NF level 1b data can be obtained by request to the corresponding author.

515 *Author contributions.* The setup of the simulations (background atmosphere, cloud scenarios, etc.) was compiled and discussed with all authors CK, SG, and RS. The simulations have been mainly performed by SG and the analysis was mainly done by CK under intensive discussions with all authors. CK wrote the manuscript with contributions of the two other authors SG and RS.

Competing interests. The authors declare that they have no competing interests.

References

Biermann, U.M.: Gefrier- und FTIR-Experimente zur Nukleation und Lebensdauer stratosphärischer Wolken, Ph.D. thesis, Universität Biele-feld, Germany, ISBN 3-89712-212-X, 1998.

Biermann, U.M., Luo, B.P., and Peter, T.: Absorption spectra and optical constants of binary and ternary solutions of H_2SO_4, HNO_3, and H_2O in the mid infrared at atmospheric temperatures, J. Phys. Chem. A, 104, 783–793, doi:10.1021/jp992349i, 2000.

Boone, C.D., Walker, K.A., Bernath, P.F.: Version 3 Retrievals for the Atmospheric Chemistry Experiment Fourier Transform Spectrometer (ACE-FTS), in: The Atmospheric Chemistry Experiment ACE at 10: a solar occultation anthology, edited by: Bernath, P.F., A Deepak Publishing, Virginia, United States of America, 103–127, 2013.

Bullister, J.: Atmospheric CFC-11, CFC-12, CFC-113, CCl_4 and SF_6 Histories., Tech. rep., Carbon Dioxide Information Analysis Center, Oak Ridge National Laboratory, US Department of Energy, Oak Ridge, Tennessee, 2011.

Dee, D.P., Uppala, S.M., Simmons, A.J., Berrisford, P., Poli, P., Kobayashi, S., Andrae, U., Balmaseda, M.A., Balsamo, G., Bauer, P., Bech-told, P., Beljaars, A.C.M., van de Berg, L., Bidlot, J., Bormann, N., Delsol, C., Dragani, R., Fuentes, M., Geer, A. J., Haimberger, L., Healy, S.B., Hersbach, H., Hólm, E.V., Isaksen, L., Kållberg, P., Köhler, M., Matricardi, M., McNally, A.P., Monge-Sanz, B.M., Mor-crette, J.-J., Park, B.-K., Peubey, C., de Rosnay, P., Tavolato, C., Thépaut, J.-N. and Vitart, F.: The ERA-Interim reanalysis: configuration and performance of the data assimilation system, Q.J.R. Meteor. Soc., 137, 553–597, doi:10.1002/qj.828, 2011.

Diallo, M., Legras, B., Ray, E., Engel, A., and Añel, J. A.: Global distribution of CO_2 in the upper troposphere and stratosphere, Atmos. Chem. Phys., 11, 3861–3878, doi:10.5194/acp-17-3861-2017, 2017.

Dudhia, A.: The Reference Forward Model (RFM), J. Quant. Spectrosc. Radiat. Transfer, 186, 243–253, 2017.

Fahey, D.W., Gao, R.S., Carslaw, K S., Kettleborough, J., Popp, P.J., Northway, M.J., Holecek, J.C., Ciciora, S.C., McLaughlin, R.J., Thompson, T.L., Winkler, R.H., Baumgardner, D.G.,Gandrud, B., Wennberg, P.O., Dhaniyala, S., McKinley, K., Peter, T., Salawitch, R.J., Bui, T.P., Elkins, J.W., Webster, C.R., Atlas, E.L., Jost, H., Wilson, J.C., Herman, R.L., Kleinböhl, A.,and von König, M.: The detection of large HNO_3 containing particles in the winter Arctic stratosphere, Science, 291, 1026–1031,2001.

Fastie, W.: Ebert Spectrometer Reflections, Phys. Today, 4, 37–43, 1991.

Fischer, H., Birk, M., Blom, C., Carli, B., Carlotti, M., von Clarmann, T., Delbouille, L., Dudhia, A., Ehhalt, D., Endemann, M., Flaud, J. M., Gessner, R., Kleinert, A., Koopman, R., Langen, J., López-Puertas, M., Mosner, P., Nett, H., Oelhaf, H., Perron, G., Remedios, J., Ri-dolfi, M., Stiller, G., and Zander, R.: MIPAS: an instrument for atmospheric and climate research, Atmos. Chem. Phys., 8, 2151–2188, doi:10.5194/acp-8-2151-2008, 2008.

Glatthor, N., von Clarmann, T., Fischer, H., Funke, B., Grabowski, U., Höpfner, M., Kellmann, S., Kiefer, M., Linden, A., Milz, M., Steck, T., and Stiller, G. P.: Global peroxyacetyl nitrate (PAN) retrieval in the upper troposphere from limb emission spectra of the Michelson Interferometer for Passive Atmospheric Sounding (MIPAS), Atmos. Chem. Phys., 7, 2775–2787, doi:10.5194/acp-7-2775-2007, 2007.

Gordley, L.L., and Russell III, J.M.: Rapid inversion of limb radiance data using an emissivity growth approximation, Appl. Optics, 20, 807–813, 1981.

Griessbach, S., Hoffmann, L., Hoepfner, M., Riese, M., and Spang, R.: Scattering in infrared radiative transfer: A comparison between the spectrally averaging model JURASSIC and the line- by-line model KOPRA, J. Quant. Spectrosc. Radiat. Transfer, 27,102–118, 2013.

Griessbach, S., Hoffmann, L., Spang, R., and Riese, M.: Volcanic ash detection with infrared limb sounding: MIPAS observations and radiative transfer simulations, Atmos. Meas. Tech., 7, 1487-1507, 2014.

Atmospheric
Measurement
Techniques
Open Access

Discussions

EGU

Griessbach, S., Hoffmann, L., Spang, R., von Hobe, M., Müller, R., and Riese, M.: Infrared limb emission measurements of aerosol in the troposphere and stratosphere, Atmos. Meas. Tech., 9, 4399–4423, 2016.

Griessbach, S., Hoffmann, L., Spang, R., Achtert, P., von Hobe, M., Mateshvili, N., Müller, R., Riese, M., Rolf, C., Seifert, P., and Vernier, J.-P.: Aerosol and cloud top height information of Envisat MIPAS measurements, Atmos. Meas. Tech., doi:10.5194/amt-13-1243-2020, 2020.

565 Grossmann, K. U., Offermann, D., Gusev, O., Oberheide, J., Riese, M., and Spang, R.: The CRISTA-2 mission, J. Geophys. Res., 107, 8173, doi:10.1029/2001JD000667, 2002.

Hoffmann, L.: Schnelle Spurengasretrieval für das Satellitenexperiment Envisat MIPAS, JUEL-4207, Forschungszentrum Jülich, Germany, ISSN 0944-2952, 2006.

Hoffmann, L., Spang, R., Kaufmann, M., and Riese, M.: Retrieval of CFC-11 and CFC-12 from Envisat MIPAS observations by means of
570 rapid radiative transfer calculations, Adv. Space Res., 36, 915–921, 2005.

Hoffmann, L., Kaufmann, M., Spang, R., Müller, R., Remedios, J.J., Moore, D.P., Volk, C.M., von Clarmann, T., and Riese, M.: Envisat MIPAS measurements of CFC-11: retrieval, validation, and climatology, Atmos. Chem. Phys., 8, 3671–3688, 2008.

Hoffmann, L., Weigel, K., Spang, R., Schroeder, S., Arndt, K., Lehmann, C., Kaufmann, M., Ern, M., Preusse, P., Stroh, F., and Riese, M.:CRISTA-NF measurements of water vapor during the SCOUT-O3 Tropical Aircraft Campaign, Adv. Space Res., 43, 74–81, 2009.

575 Hoffmann, L., and Alexander, M.J.: Retrieval of stratospheric temperatures from Atmospheric Infrared Sounder radiance measurements for gravity wave studies, J. Geophys. Res., 114, D7, D07105, 2009.

Hoffmann, L., and Riese, M.: Tomographic Retrievals for High Spatial Resolution Measurements of the PREMIER Infrared Limb Sounder, in: Proceedings of the ESA Living Planet Symposium, SP-686, ESA Publications Division, ESTEC, Keplerlaan 1, 2200 AG Noordwijk, The Netherlands, 2010.

580 Höpfner, M., Oelhaf, H., Wetzel, G., Friedl-Vallon, F., Kleinert, A., Lengel, A., Maucher, G., Nordmeyer, H., Glatthor, N., Stiller, G., v. Clarmann, T., Fischer, F., Kröger, C., and Deshler, T.: Evidence of scattering of tropospheric radiation by PSCs in mid-IR limb emission spectra: MIPA-B observations and KOPRA simulations, Geophys. Res. Lett., 29, 1278, doi:10.1029/2001GL014443, 2002.

Höpfner, M., Luo, B.P., Massoli, P., Cairo, F., Spang, R., Snels, M., Di Donfrancesco, G., Stiller, G., von Clarmann, T., Fischer, H., and Biermann, U.: Spectroscopic evidence for NAT, STS, and ice in MIPAS infrared limb emission measurements of polar stratospheric
585 clouds, Atmos. Chem. Phys., 6, 1201-1219, doi:10.5194/acp-6-1201-2006, 2006.

Kalicinsky, C., Grooß, J.-U., Günther, G., Ungermann, J., Blank, J., Höfer, S., Hoffmann, L., Knieling, P., Olschewski, F., Spang, R., Stroh, F., and Riese, M.: Observations of filamentary structures near the vortex edge in the Arctic winter lower stratosphere, Atmos. Chem. Phys., 13, 10859-10871, doi:10.5194/acp-13-10859-2013, 2013.

Kullmann, A., Riese, M., Olschewski, F., Stroh, F., and Grossmann, K. U.: Cryogenic infrared spectrometers and telescopes for the atmo-
590 sphere – new Frontiers, Proc. SPIE, 5570, 423–432, 2004.

Lowe, D., and MacKenzie, A.R.: Polar stratospheric cloud microphysics and chemistry, J. Atmos. Sol.-Terr. Phys., 70, 13–40,doi:10.1016/j.jastp.2007.09.011, 2008.

Marshall, B.T., Gordley, L.L., and Chu, D.A.: BANDPAK: Algorithms for Modeling Broadband Transmission and Radiance, J. Quant. Spectrosc. Radiat. Transfer, 52, 581–599, 1994.

595 Molleker, S., Borrmann, S., Schlager, H., Luo, B., Frey, W., Klingebiel, M., Weigel, R., Ebert, M., Mitev, V., Matthey, R., Woiwode, W., Oelhaf, H., Dörnbrack, A., Stratmann, G., Grooß, J.-U., Günther, G., Vogel, B., Müller, R., Krämer, M., Meyer, J.,and Cairo, F.: Micro-physical properties of synoptic-scale polarstratospheric clouds: in situ measurements of unexpectedly large HNO_3-containing particles in the Arctic vortex, Atmos. Chem.Phys., 14, 10785–10801, doi:10.5194/acp-14-10785-2014, 2014.

Offermann, D., Grossmann, K.-U., Barthol, P., Knieling, P., Riese, M., and Trant, R.: Cryogenic Infrared Spectrometers and Telescopes for the
600   Atmosphere (CRISTA) experiment and middle atmosphere variability, J. Geophys. Res., 104, 16311–16325, doi:10.1029/1998JD100047,
        1999.

Peter, T. and Grooß, J.-U.: Polar Stratospheric Clouds and Sulfate Aerosol Particles: Microphysics, Denitrification and Heterogeneous Chem-
        istry, in: Stratospheric Ozone Depletion and Climate Change, edited by Müller, R., Royal Society of Chemistry, 2012.

Pope, R.J., Richards, N.A.D., Chipperfield, M.P., Moore, D.P., Monks, S.A., Arnold, S.R., Glatthor, N., Kiefer, M., Breider, T.J., Harri-
605   son, J.J., Remedios, J.J., Warneke, C., Roberts, J.M., Diskin, G.S., Huey, L.G., Wisthaler, A., Apel, E.C., Bernath, P.F., and Feng, W.:
        Intercomparison and evaluation of satellite peroxyacetyl nitrate observations in the upper troposphere–lower stratosphere, Atmos. Chem.
        Phys., 16, 13541–13559, doi:10.5194/acp-16-13541-2016, 2016.

Preusse, P., Schroeder, S., Hoffmann, L., Ern, M., Friedl-Vallon, F., Ungermann, J., Oelhaf, H., Fischer, H., and Riese, M.: New perspectives
        on gravity wave remote sensing by spaceborne infrared limb imaging, Atmos. Meas. Tech., 2, 299–311, 2009.

610 Remedios, J.J., Leigh, R.J., Waterfall, A.M., Moore, D.P., Sembhi, H., Parkes, I., Greenhough, J., Chipperfield, M.P., and Hauglustaine, D.:
        MIPAS reference atmospheres and comparisons to V4.61/V4.62 MIPAS level 2 geophysical data sets, Atmos. Chem. Phys. Discuss., 7,
        9973–10017, doi:10.5194/acpd-7-9973-2007, 2007.

Riediger, O., Volk, C. M., Strunk, M., and Schmidt, U.: HAGAR – a new in situ tracer instrument for stratospheric balloons and high altitude
        aircraft, Eur. Comm. Air Pollut. Res. Report, 73, 727–730, 2000.

615 Schroeder, S., Kullman, A., Preusse, P., Stroh, F., Weigel, K., Ern, M., Knieling, P., Olschewski, F., Spang, R., and Riese, M.: Radiance
        calibration of CRISTA-NF, Adv. Space Res., 43, 1910–1917, doi:10.1016/j.asr.2009.03.009, 2009.

Solomon, S.: Stratospheric ozone depletion: A review of concepts and history, Rev. Geophys., 37, 275–315, 1999.

Spang, R., Riese, M., and Offermann, D.: CRISTA-2 observations of the south polar vortex in winter 1997: A new dataset for polar process
        studies, Geophys. Res. Lett., 25, 3159–3162, doi:10.1029/2000GL012374, 2001.

620 Spang, R., Eidmann, G., Riese, M., Offermann, D., and Preusse, P: CRISTA observations of cirrus clouds around the tropopause, J. Geophys.
        Res., 107, D23, doi:10.1029/2001JD000698, 2002.

Spang, R., and Remedios, J.J.: Observations of a distinctive infra-red spectral feature in the atmospheric spectra of polar stratospheric clouds
        measured by the CRISTA instrument, Geophys. Res. Lett., 30, 1875, doi:10.1029/2003GL017231, 2003.

Spang, R., Remedios, J.J., Kramer, L.J., Poole, L.R., Fromm, M.D., Müller, M., Baumgarten, G., and Konopka, P.: Polar stratospheric cloud
625   observations by MIPAS on ENVISAT: detection method, validation and analysis of the northern hemisphere winter 2002/2003, Atmos.
        Chem. Phys., 5, 679–692, doi:10.5194/acp-5-679-2005, 2005.

Spang, R., Hoffmann, L., Kullmann, A., Olschewski, F., Preusse, P., Knieling, P., Schroeder, S., Stroh, F., Weigel, K., and Riese, M.: High
        resolution limb observations of clouds by the CRISTA-NF experiment during the SCOUT-O3 tropical aircraft campaign, Adv. Space Res.,
        42, 1765–1775, doi:10.1016/j.asr.2007.09.036, 2008.

630 Spang, R., Arndt, K., Dudhia, A., Höpfner, M., Hoffmann, L., Hurley, J., Grainger, R.G., Griessbach, S., Poulsen, C., Remedios, J.J.,
        Riese, M., Sembhi, H., Siddans, R., Waterfall, A., and Zehner, C.: Fast cloud parameter retrievals of MIPAS/Envisat, Atmos. Chem. Phys.,
        12, 7135-7164, doi:10.5194/acp-12-7135-2012, 2012.

Spang, R., Günther, G., Riese, M., Hoffmann, L., Müller, R., and Griessbach, S.: Satellite observations of cirrus clouds in the Northern
        Hemisphere lowermost stratosphere, Atmos. Chem. Phys., 15, 927-950, doi:10.5194/acp-15-927-2015, 2015.

635   Spang, R., Hoffmann, L., Höpfner, M., Griessbach, S., Müller, R., Pitts, M.C., Orr, A.M.W., and Riese, M.: A multi-wavelength classification method for polar stratospheric cloud types using infrared limb spectra, Atmos. Meas. Tech., 9, 3619-3639, doi:10.5194/amt-9-3619-2016, 2016.

Spang, R., Hoffmann, L., Müller, R., Grooß, J.-U., Tritscher, I., Höpfner, M., Pitts, M., Orr, A., and Riese, M.: A climatology of polar stratospheric cloud composition between 2002 and 2012 based on MIPAS/Envisat observations, Atmos. Chem. Phys., 18, 5089-5113,
640   doi:10.5194/acp-18-5089-2018, 2018.

Toon, O.B., Tolbert, M.A., Koehler, B.G., Middlebrook, A.M., and Jordan, J.: Infrared optical constants of H2O ice, amorphous nitric acid solutions, and nitric acid hydrates, J. Geophys. Res., 99(D12), 25631–25654, doi:10.1029/94JD02388, 1994.

Ungermann, J., Kalicinsky, C., Olschewski, F., Knieling, P., Hoffmann, L., Blank, J., Woiwode, W., Oelhaf, H., Hösen, E., Volk, C. M., Ulanovsky, A., Ravegnani, F., Weigel, K., Stroh, F., and Riese, M.: CRISTA-NF measurements with unprecedented vertical resolution
645   during the RECONCILE aircraft campaign, Atmos. Meas. Tech., 5, 1173–1191, doi:10.5194/amt-5-1173-2012, 2012.

von Hobe, M., Bekki, S., Borrmann, S., Cairo, F., D'Amato, F., Di Donfrancesco, G., Dörnbrack, A., Ebersoldt, A., Ebert, M., Emde, C., Engel, I., Ern, M., Frey, W., Genco, S., Griessbach, S., Grooß, J.-U., Gulde, T., Günther, G., Hösen, E., Hoffmann, L., Homonnai, V., Hoyle, C. R., Isaksen, I. S. A., Jackson, D. R., Jánosi, I. M., Jones, R. L., Kandler, K., Kalicinsky, C., Keil, A., Khaykin, S. M., Khosrawi, F., Kivi, R., Kuttippurath, J., Laube, J. C., Lefèvre, F., Lehmann, R., Ludmann, S., Luo, B. P., Marchand, M., Meyer, J., Mitev, V.,
650   Molleker, S., Müller, R., Oelhaf, H., Olschewski, F., Orsolini, Y., Peter, T., Pfeilsticker, K., Piesch, C., Pitts, M. C., Poole, L. R., Pope, F. D., Ravegnani, F., Rex, M., Riese, M., Röckmann, T., Rognerud, B., Roiger, A., Rolf, C., Santee, M. L., Scheibe, M., Schiller, C., Schlager, H., Siciliani de Cumis, M., Sitnikov, N., Søvde, O. A., Spang, R., Spelten, N., Stordal, F., Sumińska-Ebersoldt, O., Ulanovski, A., Ungermann, J., Viciani, S., Volk, C. M., vom Scheidt, M., von der Gathen, P., Walker, K., Wegner, T., Weigel, R., Weinbruch, S., Wetzel, G., Wienhold, F. G., Wohltmann, I., Woiwode, W., Young, I. A. K., Yushkov, V., Zobrist, B., and Stroh, F.: Reconciliation of essential process
655   parameters for an enhanced predictability of Arctic stratospheric ozone loss and its climate interactions (RECONCILE): activities and results, Atmos. Chem. Phys., 13, 9233–9268, doi:10.5194/acp-13-9233-2013, 2013.

Waibel, A.E., Peter, T., Carslaw, K.S., Oelhaf, H., Wetzel, G., Crutzen, P.J., Pöschl, U., Tsias, A., Reimer, E., and Fischer, H.:Arctic Ozone Loss Due to Denitrification, Science, 283, 2064–2069, doi:10.1126/science.283.5410.2064, 1999.

Weigel, K.: Infrared limb-emission observations of the upper troposphere, lower stratosphere with high spatial resolution, Ph.D. thesis,
660   University of Wuppertal, Wuppertal, Germany, 2009.

Weigel, K., Riese, R., Hoffmann, L., Hoefer, S., Kalicinsky, C., Knieling, P., Olschewski, F., Preusse, P., Stroh, F., Spang, R., and Volk, C.M.: CRISTA-NF measurements during the AMMA-SCOUT-O3 aircraft campaign, Atmos. Meas. Tech., 3, 1437–1455, 2010.

Werner, A., Volk, C. M., Ivanova, E. V., Wetter, T., Schiller, C.,Schlager, H., and Konopka, P.: Quantifying transport into the Arctic lowermost stratosphere, Atmos. Chem. Phys., 10, 11623–11639, doi:10.5194/acp-10-11623-2010, 2010.

665   Woiwode, W., Höpfner, M., Bi, L., Pitts, M.C., Poole, L.R., Oelhaf, H., Molleker, S., Borrmann, S., Klingebiel, M., Belyaev, G., Ebersoldt, A., Griessbach, S., Grooß, J.-U., Gulde, T., Krämer, M., Maucher, G., Piesch, C., Rolf, C., Sartorius, C., Spang, R., and Orphal, J.: Spectroscopic evidence of large aspherical β-NAT particles involved in denitrification in the December 2011 Arctic stratosphere, Atmos. Chem. Phys., 16, 9505-9532, doi:10.5194/acp-16-9505-2016, 2016.

Woiwode, W., Höpfner, M., Bi, L., Khosrawi, F., and Santee, M.L.: Vortex-Wide Detection of Large Aspherical NAT Particles in the Arctic
670   Winter 2011/12 Stratosphere, Geophys. Res. Lett., 46, 13420– 13429, doi:10.1029/2019GL084145, 2019.

Atmospheric
Measurement
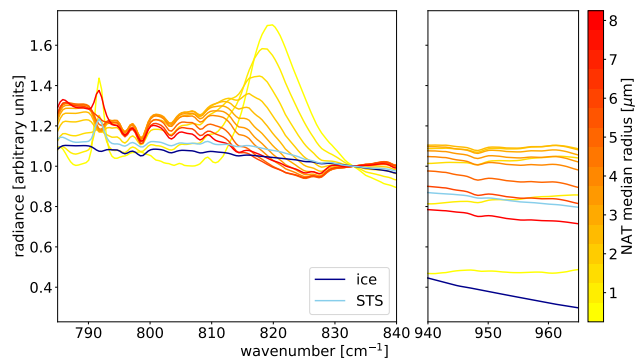Techniques
Discussions
Open Access
EGU

Figure 1. Selected simulation results for infrared spectra in the presence of polar stratospheric clouds consisting of NAT particles with different particle median radii, STS, and ice. The spectra have been scaled such that the radiance for all spectra equals 1 in the spectral window $832.0 - 834.0$ cm^{-1}.

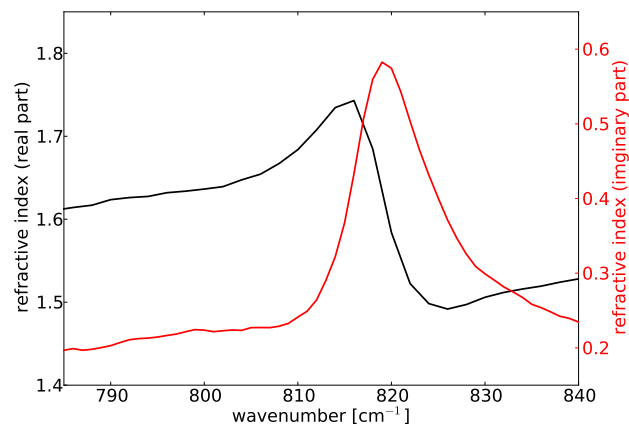**Figure 2.** Real and imaginary part of the refractive index of β-NAT by Biermann (1998) with refinement in Höpfner et al. (2006).
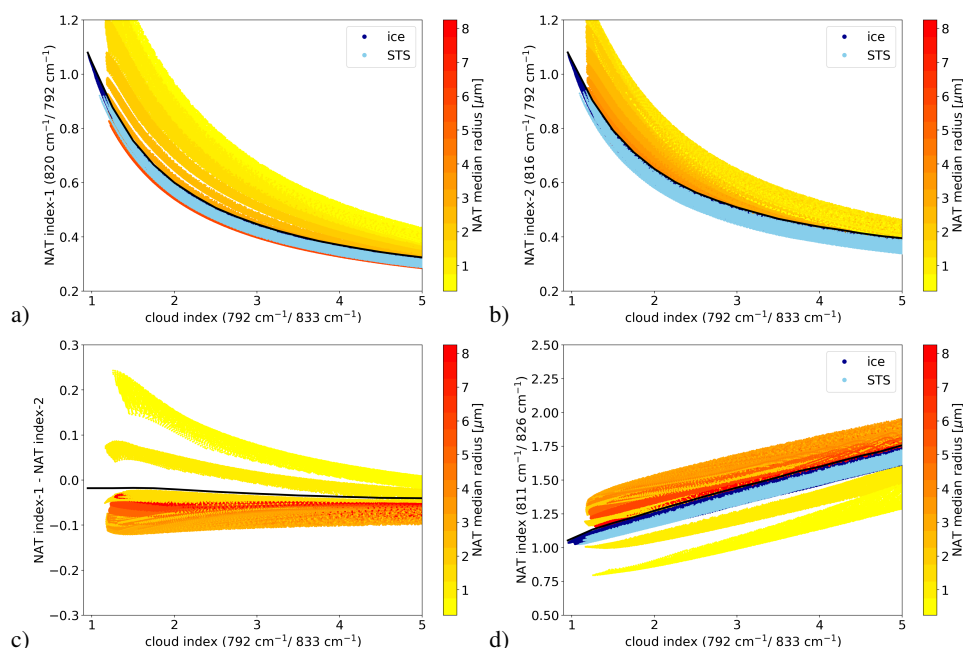
Figure 3. Scatter plots for different NAT indices versus cloud index. a) NAT index-1 $(819 - 821 \text{ cm}^{-1})/(791 - 793 \text{ cm}^{-1})$; b) NAT index-2 $(815 - 817 \text{ cm}^{-1})/(791 - 793 \text{ cm}^{-1})$; c) NAT index-1 – NAT index-2; d) NAT index-3 $(810 - 812 \text{ cm}^{-1})/(825 - 827 \text{ cm}^{-1})$. The black lines show the separation lines, which mark the upper envelope of the regions of STS and ice (in a), b), and d)) or the region of medium and large NAT (in c)). Simulation results for ice and STS are in shown in dark and light blue, respectively.
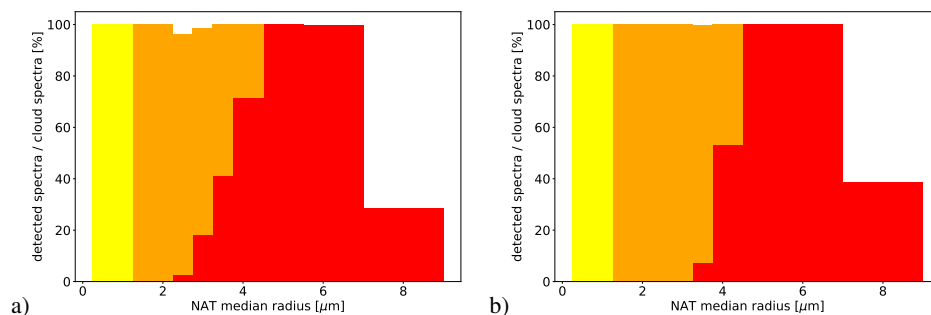
Figure 4. The histograms show the proportion of the detected spectra (NAT) per cloud spectra in each size bin of the simulations. The colours illustrate the different cases $1 - 3$. Case-1 is shown in yellow, case-2 in orange, case-3 in red. For the description of the different cases see details in text. In panel a) the CI threshold value to detect a spetrum as cloud spectrum is 5.0 (in total about 365000 cloud spectra) and in panel b) 3.0 (in total about 197000 cloud spectra).
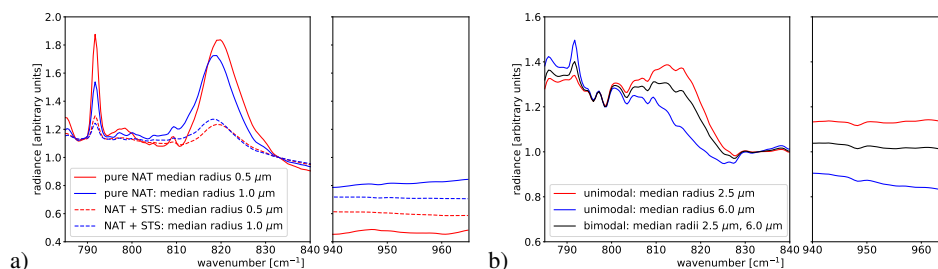
Atmospheric
Measurement
Techniques
Discussions

Figure 5. Selected spectra for NAT/STS mixed clouds (a)) and bimodal NAT particle size distributions (b)). The spectra have been scaled such that the radiance for all spectra equals 1 in the spectral window $832.0 - 834.0\ \mathrm{cm}^{-1}$. a) The solid lines show spectra for unimodal NAT particle size distributions. Red: median radius 0.5 μm and 10 ppbv HNO_3; Blue: median radius 1.0 μm and 10 ppbv HNO_3. The dashed lines show the NAT/STS mixed clouds. The amount of NAT is the same as for the pure NAT simulations and the volume density of STS is $10\ \mathrm{μm}^3/\mathrm{cm}^3$ in both cases. b) The red and blue lines show the spectra for unimodal size distributions with median radius 2.5 μm and 6.0 μm, respectivley. The amount of HNO_3 is 10 ppbv in each case. The black line shows the simulation results for a bimodal size distribution with the median radii 2.5 μm and 6.0 μm and 5 ppbv HNO_3 in each mode.
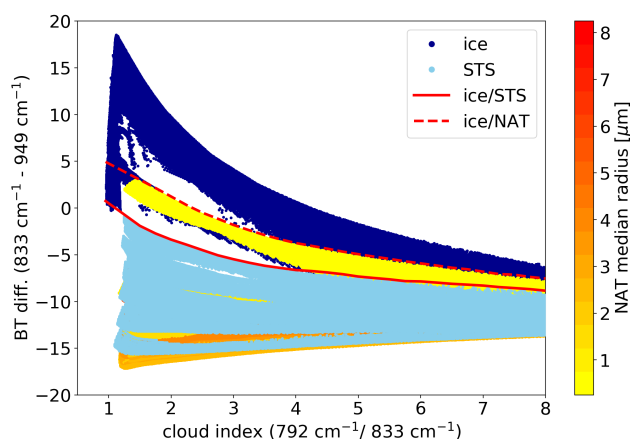

Figure 6. Scatter plot for BT difference $(832 - 834\ \mathrm{cm}^{-1}) - (947.5 - 950.5\ \mathrm{cm}^{-1})$ versus cloud index. The red solid line shows the separation line between ice and STS and the dashed line marks the separation between ice and NAT.
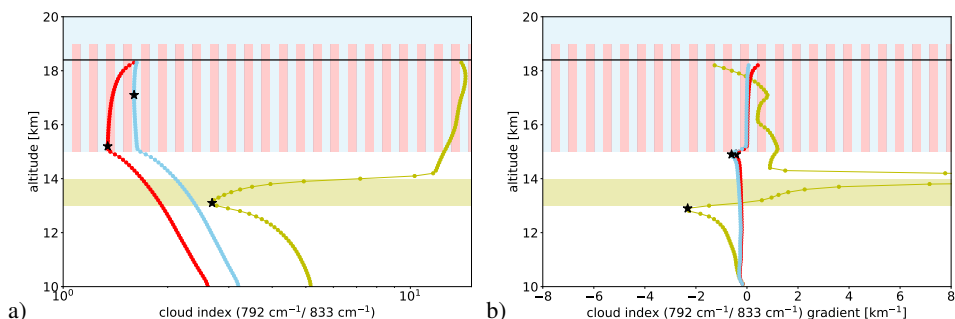
Figure 7. Vertical profiles of the cloud index (left) and the vertical gradient of the cloud index (right) for clouds with different vertical thicknesses. The colour coding shows the vertical thickness (yellow: 1 km, red: 4 km, light blue: 8 km up to 23 km). The corresponding shaded areas illustrate the vertical extent of the clouds. The black stars mark the altitudes of the CI minima and the CI gradient minima. The black horizontal line shows the flight altitude.
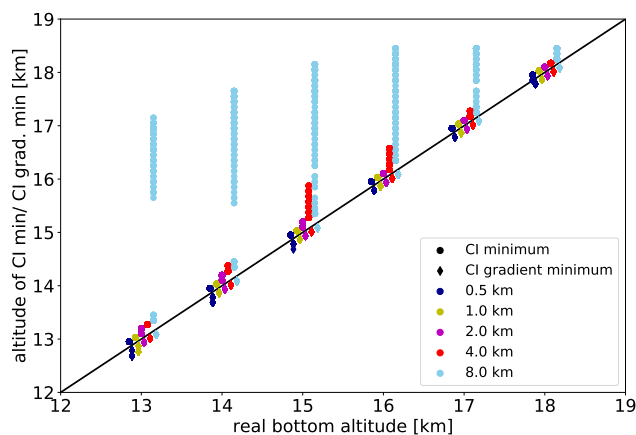

Figure 8. Altitude of CI minimum (full circles) and CI gradient minimum (full diamonds) against the real bottom altitude. The black line shows the line with slope 1. The different cloud thicknesses are shown colour coded and the points have been shifted along the line for clearness. Clouds with a CI minimum < 1.2 (optically thick) and > 5.0 (optically thin) have been excluded.
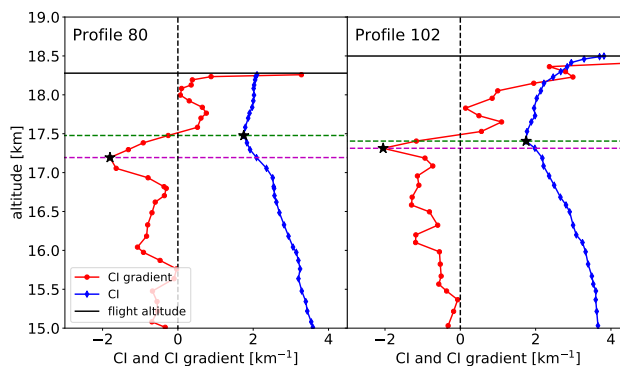
Figure 9. Altitude profiles of the cloud index (CI) and the CI gradient for two selected profiles of the CRISTA-NF measurements during RECONCILE flight 3. The CI is shown as a blue curve and the CI gradient as red curve. The flight altitude is marked by a horizontal black line. The dashed green and magenta lines show the minimum of the CI and CI gradient profile.
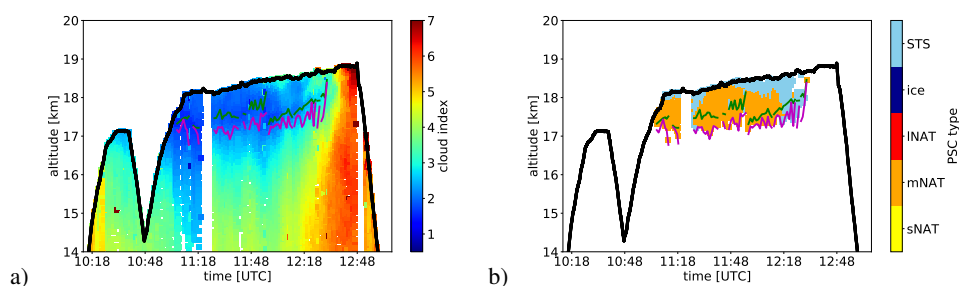

Figure 10. a) Cross section plot of the cloud index for RECONCILE flight 3. b) Cross section plot of the PSC types. The analysis of the PSC composition is performed for all spectra between flight altitude and CI gradient minimum. The black line shows the flight altitude of the aircraft. The CI minimum and the CI gradient minimum are marked by a green and a magenta line, respectively. Only profiles with a CI minimum below 3.0 and where both minima can sufficently by determined are considered.
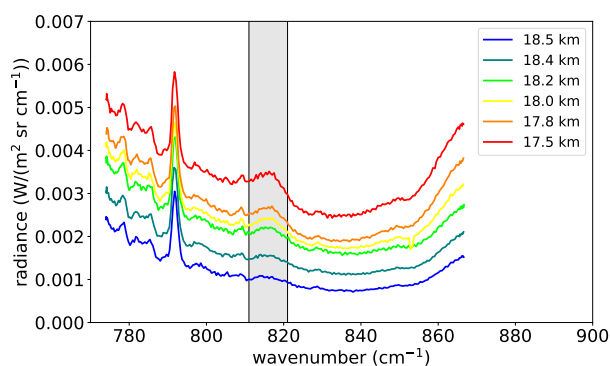

Figure 11. Example infrared spectra measured by CRISTA-NF during RECONCILE flight 3 inside PSCs at about 12:10 UTC. The spectra at different tangent altitudes are shown colour coded. The gray bar marks the region of the shifted NAT feature.

Atmospheric
Measurement
Techniques
Discussions

Table 1. Simulation properties with respect to the viewing geometry and the spectral properties

property	value
vertical sampling	100 m
spectral sampling	$0.42\ cm^{-1}$ for $785 - 840\ cm^{-1}$
	$0.59\ cm^{-1}$ for $940 - 965\ cm^{-1}$
spectral resolving power $\frac{\lambda}{\Delta\lambda}$	536 at 12.5 μm
observer altitude	18.4 km
altitude range	10 km – observer altitude

Table 2. Simulation properties with respect to background atmosphere

constituent	source	spectral region
temperature	ERA-Interim (Dee et al., 2011)	both
pressure	ERA-Interim (Dee et al., 2011)	both
CO_2	Diallo et al. (2017)	both
HNO_3	climatology	both
O_3	climatology	both
$ClONO_2$	climatology	$785–840\ cm^{-1}$
H_2O	climatology	both
HNO_4	climatology	$785–840\ cm^{-1}$
CCl_4	climatology	$785–840\ cm^{-1}$
ClO	climatology	$785–840\ cm^{-1}$
NO_2	climatology	$785–840\ cm^{-1}$
CFC-11	climatology with update (using HAGAR (Riediger et al., 2000; Werner et al., 2010) and Bullister (2011))	both
HCFC-22	climatology with update (using ACE-FTS (Boone et al., 2013))	$785–840\ cm^{-1}$
CFC-113	climatology with update (using Bullister (2011))	$785–840\ cm^{-1}$
PAN	CRISTA-NF	both
SF_6	climatology with update (using ACE-FTS (Boone et al., 2013))	$940–965\ cm^{-1}$
NH_3	climatology	$940–965\ cm^{-1}$
COF_2	climatology with update (using ACE-FTS (Boone et al., 2013) and Bullister (2011))	$940–965\ cm^{-1}$

Table 3. Cloud scenarios

cloud dimension	values	
PSC position	13.0 – 30.0 km	
PSC thickness	0.5, 1.0, 2.0, 4.0, 8.0 km	

PSC type	HNO$_3$ VMR [ppbv]* / volume density [$\mu m^3/cm^3$]**	radius [μm]
NAT	1 – 15*	0.5, 1.0, 1.5, 2.0, 2.5, 3.0,
		3.5, 4.0, 5.0, 6.0, 8.0
bimodal NAT	3/7, 5/5, 7/3* (1st/2nd mode)	1st mode: 0.5 – 2.5
		2nd mode: larger than in 1st mode
STS with wt% H$_2$SO$_4$/HNO$_3$	0.1, 0.5, 1.0, 5.0, 10.0**	0.1, 0.3, 0.5, 1.0
2/48, 25/25, and 48/2		
NAT + STS wt% 2/48	NAT: 5, 10, 15*	NAT: 0.5 – 3.5
	STS: 5.0, 10.0**	STS: 0.1, 0.3, 1.0
ice	0.1, 0.5, 1.0, 5.0, 10.0, 50.0, 100.0**	1.0, 2.0, 3.0, 4.0, 5.0, 10.0